

Effect of collisions and magnetic convergence on electron acceleration and transport in reconnecting twisted solar flare loops

M. Gordovskyy¹ · P.K. Browning¹ ·
E.P. Kontar² · N.H. Bian²

© Springer ●●●

Abstract We study a model of particle acceleration coupled with an MHD model of magnetic reconnection in unstable twisted coronal loops. The kink instability leads to the formation of helical currents with strong parallel electric fields resulting in electron acceleration. The motion of electrons in the electric and magnetic fields of the reconnecting loop is investigated using a test-particle approach taking into account collisional scattering. We discuss the effects of Coulomb collisions and magnetic convergence near loop footpoints on the spatial distribution and energy spectra of high-energy electron populations and possible implications on the hard X-ray emission in solar flares.

Keywords: Flares, Energetic Particles; Magnetic Reconnection, Theory; Energetic Particles, Acceleration

1. Introduction

Most models of particle acceleration assume that particles gain energy in the corona and then are transported into the chromosphere where they produce non-thermal radiation. This assumption follows from the standard solar flare model (*e.g.* Shibata, 1996; Yokoyama and Shibata, 1998), with the primary energy release site located above the top of a flaring loop or loop arcade. However, the standard scenario faces a number of difficulties (MacKinnon and Brown, 1989; Benka and Holman, 1994; Brown *et al.*, 2009). The main problem is the large flux of electrons required to produce the observed hard X-ray (HXR) intensity. Also, unless precipitating electrons are accompanied by ions, they may result in a strong return current, creating additional electrodynamic challenges, such as preventing the electron beam from reaching the chromosphere.

¹ Jodrell Bank Centre for Astrophysics, University of Manchester, Manchester M13 9PL, UK. email: mykola.gordovskyy@manchester.ac.uk

² School of Physics and Astronomy, University of Glasgow, Glasgow G12 8QQ, UK.

It has been suggested recently, that re-acceleration of electrons in the chromosphere may help to overcome the “number problem” (Brown *et al.*, 2009). In the proposed scenario electrons are initially accelerated in the corona and transported to the chromosphere. However, unlike in the standard thick target model (see Brown, 1971), electrons lose their energy much slower due to re-energization by the electric field in the chromosphere. Indeed, this is possible even with comparably small field strength. In the presence of Coulomb collisions, the value of electric field E required to accelerate electrons depends on their energy \mathcal{E}_e as $E = qn/(e\mathcal{E}_e)$, where q is an almost constant parameter ($q \approx 0.017\epsilon_0^{-2}e^3k_B Z \ln\Lambda$) (see *e.g.* Spitzer, 1962). Thus, for the typical chromospheric density of 10^{12} cm^{-3} , one needs a field of at least 30 V m^{-1} to accelerate electrons from 10 eV (approximately thermal energies), but only 10^{-2} V m^{-1} to accelerate electrons from 40 keV. This electric field can be achieved even with the classical resistivity provided the current density is about 1 A m^{-2} .

Particle acceleration in fragmented electric fields distributed inside flaring loops can provide another opportunity to solve the “number problem”, yielding acceleration efficiencies broadly consistent with those deduced from HXR observations. Such an acceleration model would help to reduce energy lost during particle transport and to avoid some fundamental electrodynamic issues characteristic to acceleration models involving a single localized current layer, including the return current effect (*e.g.* Knight and Sturrock, 1977) or ion-electron separation (see *e.g.* Zharkova and Gordovskyy, 2004).

There are a few previous studies of distributed particle acceleration. Vlahos, Isliker, and Lepreti (2004) considered acceleration of particles by a system of fragmented unstable current sheets derived using the cellular automata model, with a particle motion described by continuous-time random walks. Although the motion of individual particles is oversimplified, this model gives a good description of stochastic acceleration of particle population by a complex, fractal network of acceleration centres. Turkmani *et al.* (2006) investigated particle acceleration using a stationary model of the stressed coronal magnetic field. Bian and Browning (2008) used the kinetic approach to study stochastic acceleration by fluctuating fragmented electric fields in a turbulent reconnecting plasma and determined the relation between the distribution of current sheets and resulting particle energy spectra. More recently, Gordovskyy and Browning (2011, 2012) considered proton and electron acceleration in twisted coronal loops using a time-dependent three-dimensional field configuration (see also Browning *et al.*, 2011). These configurations are attractive as they are expected to be ubiquitous in the corona, as loops can be twisted by photospheric motions (see *e.g.* Brown *et al.*, 2003) or can emerge already twisted (Hood, Archontis, and MacTaggart, 2012). In any case, they contain excess magnetic energy which can be released if a loop becomes unstable.

Magnetic field convergence is expected near chromospheric footpoints of coronal loops and should have significant effect on particle motion. In the present paper we examine the effects of both magnetic field convergence and Coulomb collisions on particle acceleration and re-acceleration in twisted loops, effects which have not been considered in our previous works.

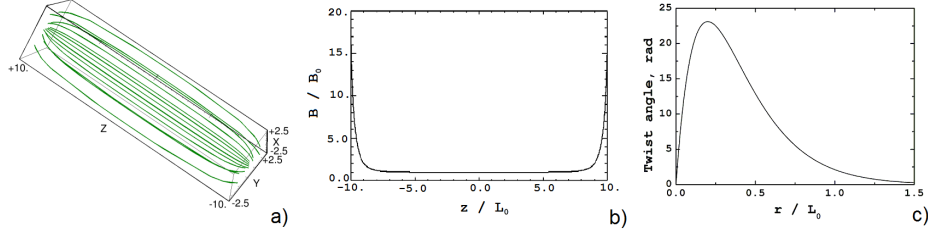


Figure 1. Initial magnetic field for the model with convergence near footpoint boundaries (panel a) and corresponding magnetic induction on the $r = 0$ axis (panel b). Panel (c) shows the final twist profile in the flux tube.

2. Evolution of twisted magnetic loop and particle motion

We consider twisted magnetic flux tube models with and without field convergence near footpoint boundaries.

Magnetic reconnection in initially cylindrical flux tubes has been extensively studied using analytical initial equilibria (Browning *et al.*, 2008; Hood, Browning, and van der Linden, 2009). These models have been already employed to study particle acceleration in Gordovskyy and Browning (2011, 2012), so that we do not discuss them further here.

A configuration with twisted magnetic field converging near footpoints can not be set up analytically. Therefore, it is derived numerically, using ideal MHD, by twisting the footpoints of an initially current-free magnetic flux tube. We use the simulation domain $x = [-5L_0; 5L_0]$, $y = [-5L_0; 5L_0]$, $z = [-10L_0; 10L_0]$. In this model scaling parameters are the same as in Gordovskyy and Browning (2012): the scale length is $L_0 = 10^6$ m, the characteristic magnetic induction is $B_0 = 4 \times 10^{-3}$ T and the characteristic density is $\rho_0 = 3.3 \times 10^{-12}$ kg m $^{-3}$; which yields the characteristic Alfvén velocity $v_0 = 1.95 \times 10^6$ m s $^{-1}$ and the characteristic timescale $t_0 = 0.53$ s.

Initially, the field is potential, formed by two point "sources" located at $\mathbf{r}_1 = \{0; 0; -10.5L_0\}$ and $\mathbf{r}_2 = \{0; 0; 10.5L_0\}$ outside the simulation domain (Figure 1a):

$$\mathbf{B}(\mathbf{r}) = B_s \left[\frac{\mathbf{r} - \mathbf{r}_1}{|\mathbf{r} - \mathbf{r}_1|^3} - \frac{\mathbf{r} - \mathbf{r}_2}{|\mathbf{r} - \mathbf{r}_2|^3} \right]. \quad (1)$$

This yields a flux tube with the magnetic field at footpoints nearly 10 times higher than the field at the centre (Figure 1b). The initial density and pressure in the MHD simulations are uniform: $\rho(t = 0) = \rho_0$ and $p(t = 0) = 5 \times 10^{-3} \mu_0^{-1} B_0^2$, *i.e.* it is magnetically dominated plasma.

The twist is introduced using the azimuthal velocity at the $z = \pm 10L_0$ boundaries (corresponding to the photospheric footpoints). The angular velocity depends on the radius as $\omega \sim r^2/r_0^2 \exp(-r/r_0)$, which is generally consistent with observed sunspot rotation (*e.g.* Gopasyuk, 1977), where $r_0 = 0.2L_0$. The corresponding twist (defined as $\phi(r, t) = \int_0^t \omega(r, t) dt$) is shown in Figure 2c. The resulting configuration (at $t = 100t_0$) has a maximum twist of approximately 7π and is nearly force-free but is, apparently, unstable: the kink instability develops at $t \approx 120t_0$.

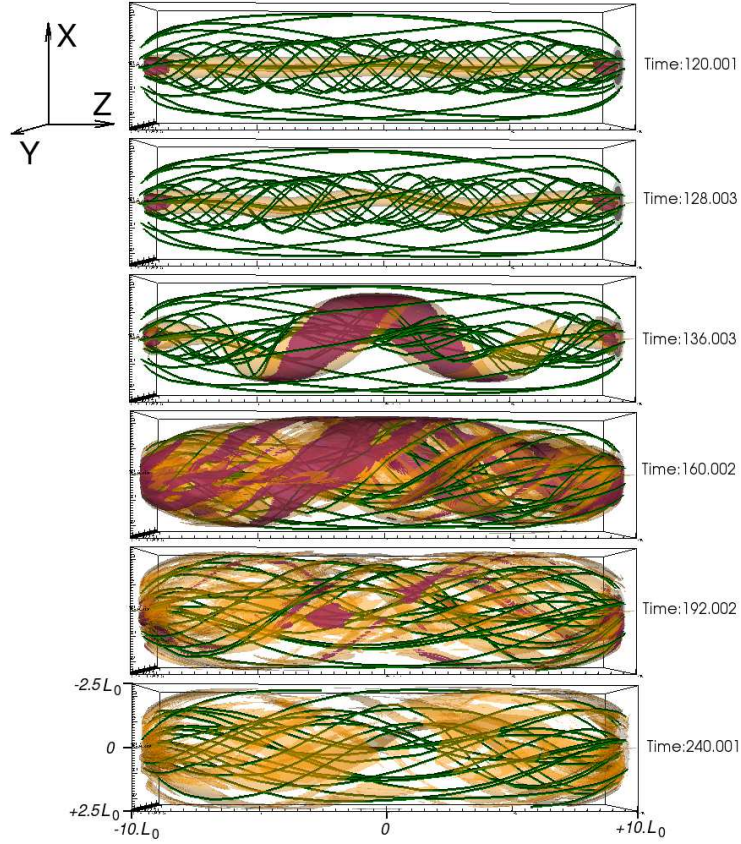


Figure 2. Evolution of magnetic field (green lines) and current density in the twisted flux tube with convergence near footpoints. Yellow and pink colours show $|j| = 4j_0$ and $|j| = 8j_0$ iso-surfaces, respectively. Times shown are in the units of t_0 .

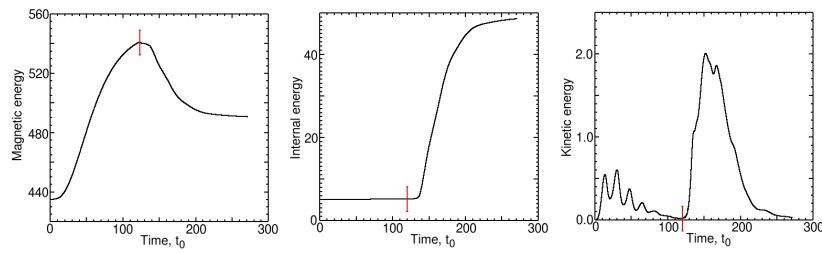


Figure 3. Variation of magnetic, kinetic and internal energies in twisted magnetic flux tube with the convergence near footpoint shown in Figure 2. Vertical dash at $t \approx 100t_0$ denotes the time when footpoint rotation stops. Energy is measured in units of $\frac{1}{2}\mu_0^{-1}B_0^2L_0^3$.

It should be noted, that this time is much shorter than realistic timescale of development of kink instability. Indeed, twisted coronal loops can remain in equilibrium for up to $10^3 - 10^4$ Alfvén times. However, since we are interested in the magnetic reconnection occurring after the loop kinks, the development of the instability is speeded up by the velocity noise (see Gordovskyy and Browning, 2011).

Further evolution of the twisted flux tube once it becomes unstable is studied using resistive MHD simulations with the Lare3D code (Arber *et al.*, 2001) (see also Gordovskyy and Browning (2011, 2012) for more details). The resistivity in this part of the simulation is non-uniform and depends on local current density as

$$\eta(j) = \begin{cases} 0 & j < j_{cr} \\ \eta_1 & j \geq j_{cr} \end{cases} \quad (2)$$

The critical current in the present simulations is $j_{cr} = 8\mu_0^{-1}B_0L_0^{-1}$ and the resistivity value is $\eta_1 = 10^{-3}L_0^2t_0^{-1}$ (which is, essentially, the inverse Lundquist number).

Magnetic field and current density evolution for the model with magnetic convergence near footpoints is shown in Figure 2, while Figure 3 shows the variation of magnetic energy E_M , kinetic energy E_K and internal energy E_I defined by following integrals over the domain volume:

$$\begin{aligned} E_M(t) &= \frac{1}{2\mu_0} \int_{\text{volume}} B^2 d\Omega \\ E_K(t) &= \frac{1}{2} \int_{\text{volume}} \rho v^2 d\Omega \\ E_I(t) &= \frac{1}{\gamma - 1} \int_{\text{volume}} p d\Omega, \end{aligned}$$

where $d\Omega$ is the elementary volume. The field and current for initially cylindrical flux tube can be seen in Gordovskyy and Browning (2011, Figures 3 and 4). It can be seen that both configurations (with and without magnetic convergence) demonstrate similar behaviour. In both cases, when the twisted flux tube kinks, the current density rapidly increases forming a helically-shaped structure. The decrease in magnetic energy at this stage is due to the dissipation of the azimuthal component of magnetic field and reconnection between twisted loop's field lines and ambient field lines. Gradually, the current distribution becomes more filamentary and the current density decreases. Reconnection stops after about $100t_0$ after kink instability occurs. During the rapid reconnection ($t = 130 - 180 t_0$, see Figure 3), the electric field in the system is order of 10^2 V m^{-1} , although it occupies only a tiny fraction of the model volume (see Gordovskyy and Browning, 2012). The main difference between the initially cylindrical configuration and one with converging field is that, in the latter case, stronger magnetic field results in substantially enhanced current density near the footpoints.

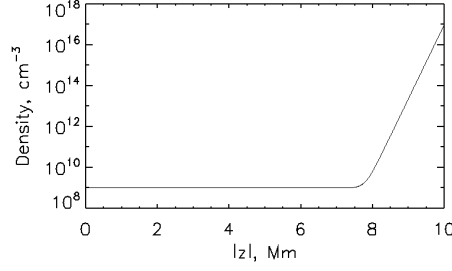


Figure 4. Density profile within the flux tube used to account for the effect of Coloumb collisions. The “coronal” part ($|z| < 7.5$ Mm) of the flux tube has a constant density of 10^9 cm^{-3} while the “chromospheric” part ($|z| = 8 - 10$ Mm) has an exponential density distribution with the scale height of about 170 km.

The obtained time-dependent electric and magnetic field configurations are used to calculate test-particle trajectories. Initially, protons and electrons in the model are uniformly distributed in the domain volume, with Maxwellian velocity distribution corresponding to $T = 0.8$ MK and an isotropic pitch-angle distribution. Since the scale-length of our MHD model is much larger than particle gyroradii, we use the relativistic guiding centre approximation to calculate particle trajectories (see Northrop, 1963):

$$\frac{d\mathbf{r}}{dt} = \mathbf{u} + \frac{\gamma(v_{\parallel})}{\gamma} \mathbf{b} \quad (3)$$

$$\mathbf{u} = \mathbf{u}_E + \frac{m}{q} \frac{(\gamma v_{\parallel})^2}{\gamma \kappa^2 B} [\mathbf{b} \times (\mathbf{b} \cdot \nabla) \mathbf{b}] + \frac{m}{q} \frac{\mu}{\gamma \kappa^2 B} [\mathbf{b} \times (\nabla(\kappa B))] \quad (4)$$

$$\frac{d(\gamma v_{\parallel})}{dt} = \frac{q}{m} \mathbf{E} \cdot \mathbf{b} - \frac{\mu}{\gamma} (\mathbf{b} \cdot \nabla(\kappa B)) + \left[\mathcal{V} \left(\frac{\delta \alpha}{\delta t} \right)_{pa} - \frac{(\gamma v_{\parallel})}{\mathcal{V}} \frac{an}{\mathcal{V}^2} \right]_{coll} \quad (5)$$

$$\frac{d\mu}{dt} = \left[(\gamma v_{\parallel}) \sqrt{\frac{2\mu}{B(1 - (\gamma v_{\parallel})^2/\mathcal{V}^2)}} - \frac{2\mu}{\mathcal{V}} \frac{an}{\mathcal{V}^2} \left(\frac{\delta \alpha}{\delta t} \right)_c \right]_{coll} \quad (6)$$

$$\gamma = \sqrt{\frac{c^2 + (\gamma v_{\parallel})^2 + 2\mu B}{c^2 - u_E^2}}, \quad (7)$$

where v_{\parallel} is the particle velocity along the magnetic field (γv_{\parallel} is treated as a single variable for the sake of convenience), and \mathbf{u} is the perpendicular velocity. The drift velocity \mathbf{u}_E is defined as $\mathbf{u}_E = \frac{\mathbf{E} \times \mathbf{B}}{B^2}$. Also, \mathbf{b} is the magnetic field direction vector $\mathbf{b} = \mathbf{B}/B$, μ is the magnetic moment defined as $\mu = \frac{1}{2}(\gamma v_g)^2/B$, γ is the Lorentz factor ($\gamma = (1 - v^2/c^2)^{-1/2}$); $\kappa = \sqrt{1 - u_E^2/c^2}$.

The terms in $[\]_{coll}$ brackets are to account for collisional energy losses and pitch-angle scattering, which are not usually incorporated in test-particle models. For typical coronal and chromospheric densities collisions are predominantly important for particles with energies in 1 – 100 keV range and, therefore, relativistic effects in the collisional terms can be ignored.

The experiments including Coulomb collisions are performed with the density profile shown in Figure 4, where the region with increasing density ($|z| = 8 \dots 10$ Mm) represents the chromosphere. Collisional energy losses are taken into account through the decrease of the particle velocity \mathcal{V} as follows:

$$\frac{d\mathcal{V}}{dt} = -a \frac{n}{\mathcal{V}^2}, \quad (8)$$

where the particle velocity for the purpose of Coulomb collisions is defined as $\mathcal{V} = \sqrt{v_{\parallel}^2 + u_g^2}$. (The drift velocity \mathbf{u} is defined solely by local field parameters and represents predominantly bulk plasma flow, and, therefore, is excluded from the collisional terms.) Here n is the ambient plasma density and a is the constant $a = 2q/m_e^2$; for typical chromospheric parameters $q = 2\pi e^4 \ln \Lambda$ is approximately $2.87 \times 10^{-12} \text{ eV}^2 \text{ cm}^2$ (Syrovatskii and Shmeleva, 1972). Essentially, this parameter determines how deep an accelerated particle can penetrate into dense plasma; in case of an uniform density the stopping depth can be evaluated as follows:

$$\left(\frac{S_{\max}}{1Mm} \right) \approx 1.75 \left(\frac{E_{\text{initial}}}{1keV} \right)^2 \left(\frac{n}{10^9 \text{ cm}^{-3}} \right)^{-1}.$$

Pitch-angle scattering is implemented through random changes of test-particle pitch-angle ratio $\alpha = \cos \theta = v_{\parallel}/\mathcal{V}$ as

$$\left(\frac{d\alpha}{dt} \right)_c = \Pi \left(dt \frac{an}{\mathcal{V}^3} \frac{1 - (\alpha + \Delta\alpha/2)^2}{\Delta\alpha^2} \right) \Delta\alpha - \Pi \left(dt \frac{an}{\mathcal{V}^3} \frac{1 - (\alpha - \Delta\alpha/2)^2}{\Delta\alpha^2} \right) \Delta\alpha, \quad (9)$$

where $\Pi(x)$ is the operator yielding 1 or 0 with the probability x or $1 - x$, respectively. Provided $\Delta\alpha$ is sufficiently small, the pitch-angle distribution evolves as

$$\frac{\partial N(E, \alpha)}{\partial t} = an\mathcal{V}^{-3} \frac{\partial}{\partial \alpha} \left((1 - \alpha^2) \frac{\partial N(E, \alpha)}{\partial \alpha} \right),$$

as expected.

In all the considered test-particle simulations we use open boundaries (*i.e.* particles are free to leave the domain; their trajectories are calculated until they cross a boundary).

3. Non-thermal electrons in a twisted coronal loop

Here we mostly focus on the spatial distribution of non-thermal electrons, which have direct implications for observations. The energy spectra of particles accelerated in initially cylindrical twisted magnetic flux tubes have been discussed by Gordovskyy and Browning (2011) and Browning *et al.* (2011). In the present paper we compare those with the energy spectra of electrons accelerated in the presence of magnetic convergence and Coulomb collisions.

The electron energy distributions (Figure 5) at the early stages of reconnection are rather similar to those obtained in simulations with no magnetic

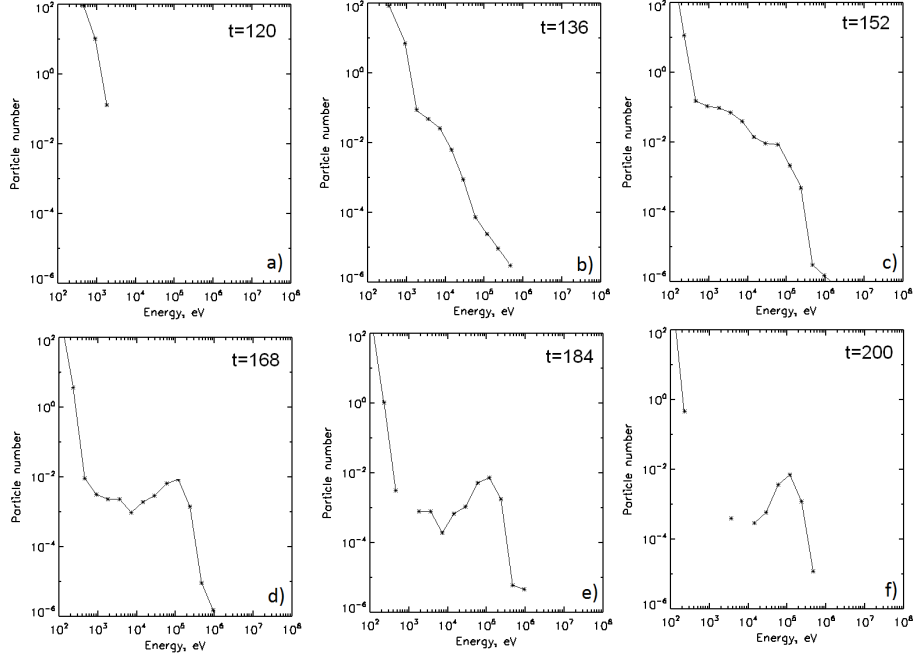


Figure 5. Energy spectra of electrons in the model with magnetic convergence and Coulomb collisions. Times (normalized by t_0) are shown in the panels. The shape of the distribution below 1 keV is not realistic on panels (b-f) (see text for details).

convergence and no collisions (Gordovskyy and Browning, 2011). Thus, during the fast energy release stage ($t = 130 - 150t_0$) the spectra are combinations of a Maxwellian thermal distribution and nearly power-law high-energy tail. However, at the later stages ($t = 150 - 250t_0$), when electric fields are gradually decaying and the collisions become dominant, the part of the spectra around few keV becomes harder and, at some point, a gap appears between the thermal part and high-energy part of the spectra. This is similar to the energy spectra of electrons precipitating in the thick-target model.

It should be noted, that the Equation (8) is valid only for non-thermal electrons (*i.e.* when $\mathcal{E}_e \gg kT$ and, therefore, the shapes of spectra in Figure 5(b-f) below 1 keV are not realistic, although the total number of “thermal” electrons is correct. This should not affect the behaviour of particles at higher energies.

Now let us consider spatial distribution of energetic electrons. The distributions of electrons with energies > 5 keV along the flaring loop are shown in the Figure 6 for three different cases. They are calculated assuming the electron populations are symmetric in respect of the loop mid-plane $z = 0$. All three distributions correspond to the stage of fast energy release in the MHD model. It can be seen that in the case of initially cylindrical flux tube, high-energy particles are nearly uniformly distributed along the reconnecting loop, which can be interpreted as the result of rather uniform distribution of strong electric field “islands” along the loop’s length. The total number of particles in this case

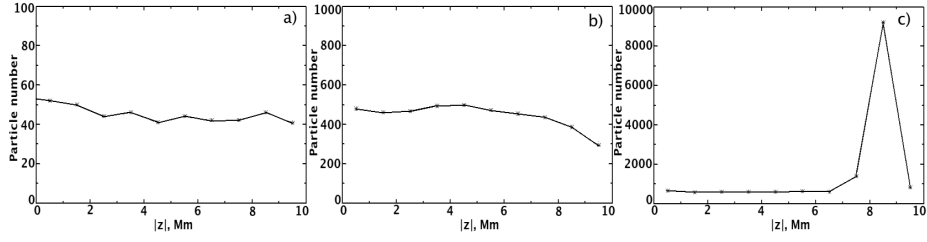


Figure 6. Distribution of electrons with energies $\mathcal{E} > 5$ keV along the flux tube. Here $z = 0$ corresponds to the centre of the flux tube and $|z| = 10 L_0$ corresponds to the footpoints. Panel (a) is for the initially cylindrical flux tube, panel (b) is for the case with convergence near footpoints, panel (c) is for the case with magnetic convergence and Coulomb collisions. All the distributions correspond to the stage of rapid energy release in the MHD simulations.

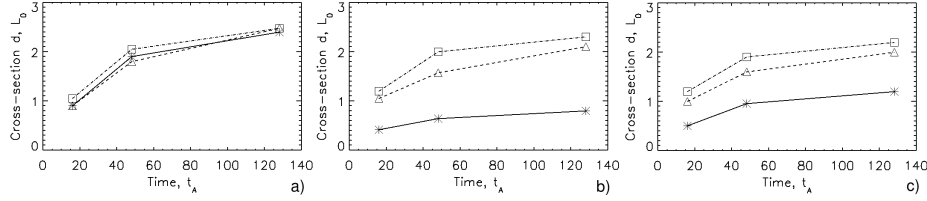


Figure 7. Variation of cross-section of the volume occupied by high-energy electrons. Panel (a) is for the initially cylindrical flux tube, panel (b) is for the case with convergence near footpoints, panel (c) is for the case with magnetic convergence and Coulomb collisions. Solid lines are for the region $|z| = 8L_0 \dots 10L_0$, dashed lines are for $|z| = 4L_0 \dots 6L_0$, dot-dashed lines are for central region $|z| < 2L_0$. Horizontal axis shows the time after onset of reconnection. (It should be noted that speed of reconnection in the models in the case (a) and in the case (b-c) can be slightly different and, therefore, times shown in panel (a) may correspond to slightly different phase compared to panels (b) and (c).) The shape of cross-section is determined visually (as it has quite sharp edges, see Gordovskyy and Browning, 2011), the size is defined as average diameter from two measurements, in x- and y- directions.

is quite low because most electrons quickly get to one of the boundaries and leave the domain.

In the case with converging magnetic field near footpoint boundaries high-energy electrons are rather uniformly distributed around the centre of the flux tube, but with some deficit close to the footpoints. This deficit is quite surprising, as one would expect a higher number of particles in these regions: particles are slowing down in stronger field and would spend more time near these boundaries. Apparently, the deficit is caused by more efficient acceleration due to stronger electric fields in these regions (see Section 2).

In the case with magnetic convergence and Coulomb collisions the majority of the electrons are located near the footpoints, which indicates that test-particles spend most of their time moving through the dense plasma representing the chromosphere. This phenomenon might be explained as the result of simultaneous action of three different effects: the converging magnetic field leads to high pitch-angles (*i.e.* $u_g > v_{||}$), which, along with collisional deceleration, prevents majority of electrons from escaping into central region of the flux tube or outside. At the same time, electrons do not thermalize completely as they are accelerated by direct electric field.

In our previous paper (Gordovskyy and Browning, 2012) we show that the cross-section of the volume occupied by accelerated particles increases with time. This happens due to the reconnection between magnetic field of twisted loop and the ambient magnetic field. Let us now examine how the cross-section sizes change with time at different distances from loop footpoints, in the three different models (Figure 7).

It can be seen that in the case of an initially cylindrical flux tube the centre and the footpoints regions expand in the same way. Cross-section diameters increase from $\approx 1L_0$ to $\approx 2.5L_0$ within $120t_0$. In the case with field convergence, the central region expands nearly at the same rate as the footpoint regions. Thus, around $z = 0$ the cross-section of the volume occupied by high-energy particles increases from $\approx 1.2L_0$ to $\approx 2.3L_0$ within about $100t_0$, while the region between $|z| = 8...10L_0$ expands from $0.4L_0$ to $0.7L_0$.

With Coulomb collisions taken into account, the footpoint sizes expand faster: the cross-section of the volume between $|z| = 8...10L_0$ increases from $0.5L_0$ to $\approx 1.2L_0$ compared with the increase from $1.2L_0$ to $2.2L_0$ near the centre of the flux tube. One of the possible explanations for this effect is strong pitch-angle scattering leading to a wider spread of particles in radial direction.

The radial expansion of the volume occupied by particles should result in the increase of the radial size of non-thermal hard X-ray sources observed in solar flares. Recent observations by Kontar *et al.* (2010) and Kontar, Hannah, and Bian (2011) show that this expansion may be happening in solar flares and the observed pace of expansion is comparable to what is seen in the numerical experiments.

4. Summary

In this paper we present preliminary results concerning electron acceleration in a kink unstable twisted coronal loop. For this purpose a model of twisted magnetic flux tube with the field convergence near its footpoints was developed using ideal MHD simulations. Further development of the kink instability resulting in magnetic reconnection and fast energy release was investigated using resistive MHD simulations with non-uniform resistivity. We formulated a set of relativistic gyro-kinetic equations taking into account energy losses and pitch-angle scattering due to Coulomb collisions and, based on the developed MHD model, studied electron acceleration during magnetic reconnection in twisted magnetic flux tube.

The considered reconnection scenario appears to be an effective particle accelerator. Taking into account scaling parameters ($\mathcal{E}_0 = 1/2 B_0^2/\mu_0 L_0^3 \approx 6 \times 10^{18}$ J, $t_0 \approx 0.53$ s) one can estimate the total energy released during the reconnection. In the case of twisted magnetic flux tube with convergence near footpoints there is $\approx 3 \times 10^{20}$ J released during ≈ 50 s. The efficiency of particle acceleration, which strongly depends on the resistivity in these models, is quite low: approximately 5–7% of the total energy released is carried by accelerated particles. This, along with the fact that the magnetic reconnection occurs in rather simple single-loop configuration, makes this model comparable to small self-contained flares

(Aschwanden *et al.*, 2009). We emphasize, however, that all these estimations are subject to the scaling parameters.

The considered electron acceleration model is quite attractive because the particle acceleration is not localized at the top of the loop but occurs along the whole loop length, including the chromosphere.

The considered model yields number of observational implications. The main feature is expansion of the column occupied by high-energy particles in radial direction. Taking into account recent progress in determination of geometric properties of hard X-ray sources (Kontar *et al.*, 2010; Battaglia and Kontar, 2011), this feature can be used as an observational test for this sort of models. However, more simulations are needed to investigate this reconnection and acceleration scenario with wider range of parameters.

Acknowledgements This work is supported by the Science and Technology Facilities Council (UK). Computational facilities have been provided by the UK MHD Consortium. Financial support by the European Commission through the HESPE Network is gratefully acknowledged.

References

- Arber, T.D., Longbottom, A.W., Gerrard, C.L., Milne, A.M.: 2001, *J. Comput. Phys.* **171**, 151.
- Aschwanden, M.J., Wuelser, J.P., Nitta, N.V., Lemen, J.R.: 2009, *Solar Phys.* **256**, 3. doi: 10.1007/s11207-009-9347-4
- Battaglia, M., Kontar, E.P.: 2011, *Astrophys. J.* **735**, 42.
- Benka, S.G., Holman, G.D.: 1994, *Astrophys. J.* **435**, 469.
- Bian, N.H., Browning, P.K.: 2008, *Astrophys. J.* **687**, L111.
- Brown, D.S., Nightingale, R.W., Alexander, D., Schrijver, C.J., Metcalf, T.R., Shine, R.A., Title, A.M., Wolfson, C.J.: 2003, *Solar Phys.* **216**, 79. doi: 10.1023/A:1026138413791
- Brown, J.C.: 1971, *Solar Phys.* **18**, 489. doi: 10.1007/BF00149070
- Brown, J.C., Turkmani, R., Kontar, E.P., MacKinnon, A.L., Vlahos, L.: 2009, *Astron. Astrophys.* **508**, 993.
- Browning, P.K., Gerrard, C., Hood, A.W., Kevis, R., van der Linden, R.A.M.: 2008, *Astron. Astrophys.* **485**, 837.
- Browning, P.K., Gordovskyy, M., Stanier, A., Hood, A.W., Dalla, S.: 2011, *Plasma Phys. Contr. Fusion*, **53**, 124030.
- Gopasyuk, S.I.: 1977, *Izv. Crimean Astr. Obs.*, **57**, 107.
- Gordovskyy, M., Browning, P.K.: 2011, *Astrophys. J.* **729**, 101.
- Gordovskyy, M., Browning, P.K.: 2012, *Solar Phys.*, **277**, 299. doi: 10.1007/s11207-011-9900-9
- Hood, A.W., Browning, P.K., van der Linden, R.A.M.: 2009, *Astron. Astrophys.* **506**, 913.
- Hood, A.W., Archontis, V., MacTaggart, D.: 2012, *Solar Phys.*, **278**, 3. doi: 10.1007/s11207-011-9745-2
- Knight, J.W., Sturrock, P.A.: 1977, *Astrophys. J.*, **218**, 306.
- Kontar, E.P., Hannah, I.G., Jeffrey, N.L.S., Battaglia, M.: 2010, *Astrophys. J.* **717**, 250.
- Kontar, E.P., Hannah, I.G., Bian, N.H.: 2011, *Astrophys. J.* **730**, L22.
- MacKinnon, A.L., Brown, J.C.: 1989, *Solar Phys.* **122**, 303. doi: 10.1007/BF00912997
- Northrop, T.: 1963, *The Adiabatic Motion of Charged Particles*, Interscience, New York, p.32.
- Shibata, K.: 1996, *Adv. Space Res.* **17**, 9.
- Spitzer, L.: 1962, *Physics of fully ionized gases*, Interscience, New York.
- Syrovatskii, S.I., Shmeleva O.P.: 1972 *Sov. Astron.* **16**, 273.
- Turkmani, R., Cargill, P.J., Galsgaard, K., Vlahos, L., Isliker, H.: 2006, *Astron. Astrophys.* **449**, 749.
- Vlahos, L., Isliker, H., Lepreti, F.: 2004, *Astrophys. J.*, **608**, 540.
- Yokoyama, T., Shibata, K.: 1998, *Astrophys. J.* **494**, L113.
- Zharkova, V.V., Gordovskyy, M.: 2004, *Astrophys. J.* **604**, 884.

